FACILE SOL-GEL SYNTHESIS OF SILICA SORBENTS FOR THE REMOVAL OF ORGANIC POLLUTANTS FROM AQUEOUS MEDIA

Ana L.M. Gomes[1], Pedro H.M. Andrade[1,2], Hugo G. Palhares[1], Marcello R. Dumont[3], Daniel C.F. Soares[4], Christophe Volkringer[5], Manuel Houmard[6], Eduardo H.M. Nunes[1*]

(1) Departamento de Engenharia Metalúrgica e de Materiais, Universidade Federal de Minas Gerais, Pampulha, CEP: 31270-901, Belo Horizonte, MG, Brasil.

(2) Laboratoire de Spectroscopie pour les Interactions, la Réactivité et l'Environnement; Université de Lille, 59655 - Villeneuve d'Ascq, France.

(3) Departamento de Engenharia de Materiais, Centro Federal de Educação Tecnológica de Minas Gerais, Nova Suíça, CEP: 30421-169, Belo Horizonte, MG, Brasil.

(4) Laboratório de Bioengenharia, Universidade Federal de Itajubá, Campus Itabira, CEP: 35903-087, Itabira, MG, Brasil.

(5) Univ. Lille, CNRS, Centrale Lille, Univ. Artois, UMR 8181 - UCCS - Unité de Catalyse et Chimie du Solide, F-59000 Lille, France.

(6) Departamento de Engenharia Química, Universidade Federal de Minas Gerais, Pampulha, CEP: 31270-901, Belo Horizonte, MG, Brasil.

* eduardo.nunes@demet.ufmg.br

ABSTRACT

In this work, silica-based adsorbents were prepared by a facile and straightforward sol-gel route. The adsorption capacity of the prepared materials was investigated using methylene blue (MB) and metamizole (sodium dipyrone – DIP) as reference pollutants. We observed that the samples prepared here, regardless of the absence of catalyst, templating agent, or heat treatment step during their preparation, are promising materials for adsorption purposes. The adsorption kinetics was investigated based on the pseudo-first and pseudo-second-order kinetic laws of Lagergren. The most promising sample showed an adsorption capacity of 36.9 $mg.g^{-1}$ (removal capacity of 92.3 %) for MB and 8.5 $mg.g^{-1}$ (20.5 %) for DIP in aqueous media kept at a pH = 7.0. We observed that the adsorption of these species is strongly associated with the electrostatic interaction between the pollutant molecules and the silica surface. Such an interaction was increased when the pH of the solution increased from 3.0 to 4.5, 7.0, or 9.0. The incorporation of amino groups derived from (3-Aminopropyl)triethoxysilane (APTES) increased the affinity of silica for MB and DIP. These functional groups were incorporated into silica via post-grafting and co-condensation. Furthermore, it was shown that the silica matrices tested here can be easily regenerated by heat treatment in air at 450 °C for periods as short as 15 min, allowing its reuse in subsequent adsorption cycles.

KEYWORDS: facile synthesis; mesoporous silica; organic pollutants; water treatment; adsorption; thermal regeneration.

1. INTRODUCTION

The consumption of pharmaceutical and personal care products (PPCPs) has increased in recent decades due to the growth of the world population, higher investments in the health care sector, and the aging process in industrialized countries [1]. These drugs are partially absorbed and partially excreted by humans and animals when consumed, causing the contamination of soil and water bodies. The incorrect disposal of unused medicines is also an important source of contamination. Quadra *et al.* [2] recently investigated the habits of consumption and disposal of unused medications by Brazilian citizens. They observed that around 66 % of the respondents dispose of their medicines in household trash. Analogous results were also reported by other authors [3]. This behavior is strongly related to the lack of protocols and regulations for the discharge of unused drugs in many countries. The lack of treatment plants capable of completely removing such pollutants from sewage causes them to reach the groundwater, rivers, and seas [4]. Beek *et al.* [5] detected these pollutants in sewage, surface water, groundwater, tap/drinking water, soil, and other environmental matrices, revealing their high capacity to spread in nature. It is also well established that these pollutants affect the environment and wildlife [6–8]. It should also be emphasized that the COVID-19 pandemic has increased the consumption of these drugs, which drives the conduct of studies focused on the remediation of these pollutants in water bodies. The academic community has shown great concern about the increasing concentration of these drugs in urban sewage and the environment [9].

Organic dyes are also pollutants of great concern nowadays [10]. Several sectors use these compounds, including the paper, food, textile, plastics, cosmetics, and paint

industries [11]. More than 100,000 different dyes are commercially available, and about 700,000 tons of these materials are produced every year. Around 100 tons are discharged as wastewaters each year due to the dyeing process [12]. When released in rivers and seas, the intense coloration of such pollutants inhibits the transmission of sunlight into water bodies, which negatively affects the photosynthetic activity of water-dwelling organisms [13]. Furthermore, the biological oxidation of these pollutants consumes oxygen dissolved in water, causing adverse health effects in humans and animals. They can also cause breathing difficulties, nausea, skin irritation, cancer, and genetic mutations [14].

Several strategies have been used for treating wastewaters contaminated with organic pollutants, including ozonation [15], electrochemical oxidation [16], photocatalysis [17–21] filtration [22,23], and adsorption [24,25]. Among these technologies, adsorption deserves to be highlighted due to its low environmental impact, operational ease, low cost, and efficiency [26–28]. Silica is a versatile material, widely used in a range of applications, including catalytic supports [29,30], optical glasses [31], thermal insulators [32], and sorption [33–35]. Among the preparation methods commonly used for obtaining silica, the sol-gel process provides a flexible chemical route to prepare materials with tailored properties such as particle size, surface chemistry, and pore structure. Moreover, this technique exhibits lower synthesis temperatures and shorter reaction times compared to other processing methods. Another convenient feature of this technology is related to the fact that sol-gel samples can be obtained as bulks, thin films, and powders [36].

We prepared in this work silica-based sorbents by a facile sol-gel route where no catalyst, surfactant, or heat treatment step was used. These materials were used to treat aqueous solutions containing either methylene blue (MB) or metamizole, also known as dipyrone (DIP) or Novalgin®. MB is a dye widely used for dyeing cotton, wool, and silk [37]. It is highly resistant to biodegradation and very stable to light and oxidation. Besides, it is a toxic, persistent, carcinogenic, and mutagenic compound [38]. In Brazil, the textile industry is among the most important sectors when considering the number of jobs and investment volume. In addition, it has been reported that the discharge of colored wastewater has increased considerably in recent decades in Brazil, which aggravates environmental problems [39]. On the other hand, DIP is a pyrazolone derivative, widely used as an over-the-counter analgesic and antipyretic in Europe, Africa, and South America [40]. It is mainly marketed in sodium form in different pharmaceutical formulations, including oral solutions, tablets, injectables, and suppositories [41]. It is possible to purchase DIP in Brazil without a prescription, which contributes to its widespread use. Some materials prepared here were modified with amino groups to improve their chemical affinity with MB and DIP [42,43]. We applied kinetic models to the adsorption curves and investigated the thermal regeneration of the prepared adsorbents. The pore network and chemical structure of these samples were examined in depth by several techniques. This work provides new insights into the preparation and use of silica sol-gel to remove organic pollutants from aqueous media. The simple preparation route suggested here deserves to be highlighted because many papers available in the literature use multi-step, complex, and time-consuming methods to prepare silica-based adsorbents.

2. MATERIALS AND METHODS

2.1 SYNTHESES

- SILICA MATRICES

Polymeric sol-gel silica solutions were initially prepared following a methodology similar to those described elsewhere [44–46]. Nonetheless, we used longer stirring times (24 h versus 30 min) in this work, which favors the complete hydrolysis of the silicon precursor before condensation takes place. In this process, we initially prepared a solution of deionized Milli-Q water (H_2O) and absolute ethanol (EtOH, Synth, 99.5 vol.%) under stirring at room temperature. Tetraethyl orthosilicate (TEOS, Merck, 98 vol.%) was then dripped into the solution and kept under stirring at room temperature for 24 h. The molar ratio of TEOS: EtOH: H_2O is adjusted to 1: 4: x, where x is 4, 10, or 20. The as-prepared solution was aged in a closed flask for 24 h at 90 °C. The obtained gel was washed with H_2O and air-dried at 80 °C for 4 days. The washing step is imperative for removing residual ethoxy groups from the prepared gels. It is worth highlighting that these materials were prepared without using acidic or basic catalysts and that no heat treatment steps were employed: these samples were only air-dried at 80 °C. The as-prepared materials were subsequently powdered in an agate mortar.

Mesoporous silica samples with ordered pore networks (SBA-16, Santa Barbara Amorphous) were also prepared in this study for reference purposes. These materials have been widely used in the adsorption of organic pollutants [47,48]. They were obtained as follows. Poly (ethylene oxide)-poly (propylene oxide)-poly (ethylene oxide)

triblock copolymer (Pluronic® F127, Merck, M_w = 12,600 g.mol^{-1}) was initially dissolved at room temperature under stirring for 2 h in a solution of H_2O and hydrochloric acid (HCl, Synth, 37 vol.%). The concentration of HCl in this solution was 1.5 mol.L^{-1}. Next, TEOS was dropwise added to this acidic solution under continuous stirring at room temperature, and the as-obtained solution was kept under this condition for 24 h. The prepared sol had the following molar ratio: 1 TEOS: 147 H_2O: 4 HCl: 0.008 F127. It was then aged in air at 80 °C for 24 h. The obtained solid was washed with H_2O and EtOH and then air-dried overnight at 80 °C. Subsequently, it was heat-treated in air at 500 °C (10 °C.min^{-1}) for 6 h to remove Pluronic® F127 from silica. The removal of this template is mandatory to prepare samples with an open and ordered mesoporous structure.

- AMINE-CONTAINING SAMPLES

As mentioned before, amine-containing samples were prepared to enhance the chemical affinity of sol-gel silica with MB and DIP [42,43]. (3-Aminopropyl)triethoxysilane (APTES, Merck, ≥ 98 vol.%) was employed as the amine source in these syntheses. We used two different approaches to incorporate the amino groups into silica: post-grafting and co-condensation methods.

- Post-grafting method

The post-grafting method was conducted as follows. The previously prepared silica samples were initially kept under stirring in an aqueous HCl solution (0.2 M) at 80 °C for 2 h, washed with H_2O, and then air-dried at 60 °C overnight. This step has been

reported to be essential for activating silica before incorporating amino groups on its surface [49]. Next, 1 g of silica was mixed with 5 mL of APTES and 100 mL of anhydrous Toluene (Tol, Synth, 99.9 vol.%). This mixture was kept under stirring at 80 °C for about 6 h. The excess of APTES present on the silica surface was removed by vacuum filtration with Tol and EtOH. The excess of APTES can block the pore structure of silica, negatively affecting its adsorption capacity. The obtained materials were subsequently air-dried at 60 °C for 24 h.

- Co-condensation method

The co-condensation method was carried out following a methodology similar to that suggested by Barczak *et al.* [50]. This approach consisted of adding APTES about 40 min after TEOS during the preparation of the silica matrices. This addition of these precursors at different times is due to the faster hydrolysis kinetics of APTES compared to TEOS [51]. The molar ratio of TEOS: APTES was adjusted to 9: 1. The as-prepared solution was kept under stirring at room temperature for 24 h. The removal of Pluronic® F127 from SBA-16_Co was performed with EtOH using a tip sonicator (Hielscher UP200S) operating at 24 kHz for about 40 min. We used 200 mL of EtOH for each 1 g of silica. The samples obtained in this work are summarized in Table 1. As discussed later, MESO C and SBA-16 were chosen for the modification step with amino groups because they were the silica matrices with the highest adsorption capacities.

2.2 CHARACTERIZATIONS

FTIR was conducted on a Bruker Alpha spectrometer using an attenuated total reflectance (ATR) accessory and a diamond crystal as the reflective element. The spectra were taken at a resolution of 4 cm^{-1} and 128 scans. They were then normalized using the absorption band at 460 cm^{-1} as the reference. TG was carried out on a Shimadzu DTG-60H thermal analyzer at 10 °C.min^{-1} under nitrogen flow (20 mL.min^{-1}). The concentration (C – mmol.g^{-1}) of amino groups in the silica samples was evaluated from Equation (1), where "Loss" represents the mass loss (%) observed in the temperature range of 390-650 °C [49].

$$C = \frac{Loss}{100} \times \frac{1\ mol}{58\ g} \times \frac{1000\ mmol}{1\ mol} \quad (1)$$

N_2 sorption was conducted at -196 °C on a Quantachrome Nova 2200e system using specimens degassed under a secondary vacuum at 110 °C for up to 24 h. These tests were conducted with an experimental error of 5 %. The specific surface area (SSA – $m^2.g^{-1}$) of the examined materials was assessed by the multipoint BET (Brunauer-Emmett-Teller) method. The mean pore size (ϕ – nm) was evaluated from Equation (2), where V_{mes} ($cm^3.g^{-1}$) is the specific volume of mesopores assessed by the BET method.

$$\phi = \frac{4V_{mes}}{SSA} \quad (2)$$

SEM was performed using a Shimadzu SSX-550 microscope at an accelerating voltage of 15 kV. The samples examined by SEM were previously sputter-coated with a gold layer to prevent the accumulation of surface charges. TEM was conducted on a Tecnai G2-20 – SuperTwin FEI microscope at an accelerating voltage of 200 kV. The materials

used in TEM were previously dispersed in acetone under sonication at room temperature for 5 min and then dripped on carbon-coated grids. They were subsequently dried in air at room temperature and then examined. The Zeta potential of aqueous solutions containing the samples prepared in this work was determined on a Brookhaven ZetaPlus system. These tests were conducted in a pH range of 2-9 using sodium chloride (NaCl, Synth) as the electrolyte (10 mM). The analyzed samples were initially dispersed in a previously prepared aqueous NaCl solution. After stabilization, the pH was adjusted by dripping aqueous solutions (0.1 $mol.L^{-1}$) of ammonium hydroxide (NH_4OH, Synth) and nitric acid (HNO_3, Synth).

2.3 SORPTION TESTS

Adsorption tests were carried out using aqueous solutions containing either MB (Synth) or DIP (Hebei Jiheng Pharmaceutical) for about 4 days. We kept the concentration of MB and DIP constant at 100 $mg.L^{-1}$, while the silica loading was adjusted to 2.5 $g.L^{-1}$. Such tests were performed at room temperature and under continuous stirring. The initial pH of the water-based solutions containing MB or DIP was about 6. The concentration of MB and DIP was determined by UV-Vis spectroscopy on a Shimadzu UV-2600 spectrometer at a resolution of 0.5 nm. Aliquots collected from the solutions were centrifuged at 3400 rpm for 10 min to avoid interferences associated with suspended particles. The particle-free supernatant was diluted with deionized H_2O (each 1 mL of solution was diluted with 9 mL of H_2O) and then transferred to quartz cuvettes and examined by UV-Vis spectroscopy. The light absorption at 235 nm and 664 nm was used as the reference for DIP and MB, respectively. The uptake of these pollutants (q_t – $mg.g^{-1}$) was calculated from Equation (3), where C_i and C_t represent the initial

concentration and concentration at time t (mg.L^{-1}) of these compounds, V is the solution volume (L), and m is the adsorbent mass (g).

$$q_t = (C_i - C_t) \times \frac{V}{m} \quad (3)$$

The removal efficiency (%) was determined by Equation (4):

$$\text{Removal} = \left(\frac{C_i - C_t}{C_i}\right) \times 100\% \quad (4)$$

The thermal regeneration of the materials used in the adsorption tests was performed by heat treatment in air at 450 °C for 15 min. As discussed later, this step allowed the reuse of these materials in subsequent adsorption tests without impairing their uptake capacity.

3. RESULTS AND DISCUSSION

3.1 STRUCTURAL CHARACTERIZATION

Figure S1 exhibits TEM micrographs obtained for SBA-16. It can be observed that this material has a highly-ordered pore network, which is in line with a previous study [46]. A similar pore organization was not observed for the other silica matrices prepared in this work, which was already expected since no template was employed in their preparation. Figure 1 shows the FTIR spectra of pure and amine-loaded samples. The absorption bands at 460 cm^{-1}, 800 cm^{-1}, and 1050 cm^{-1} are ascribed to Si–O bonds [52].

The band at 560 cm^{-1} is related to siloxane rings, while that at 960 cm^{-1} is attributed to surface silanol groups (Si-OH) [53]. The bands at 690 cm^{-1}, 1366 cm^{-1}, and 1435 cm^{-1} have been ascribed to N–H bonds, CH_3 groups, and C–C bonds [54,55]. The observation of the bands at 1366 cm^{-1} and 1435 cm^{-1} for pure samples can be related to organic residues derived from the sol-gel process. The absorption bands at 1630 cm^{-1} and 1737 cm^{-1} are due to physisorbed water [56] and C=O bonds from carboxyl groups bonded to silanol and other polar groups [57]. The features at 1215 cm^{-1} and 1366 cm^{-1} are related, respectively, to C–H and C–C bonds [58]. The bands at 2870 cm^{-1} and 2930 cm^{-1} are related to C–H bonds from APTES [59]. The absorption band at 2970 cm^{-1} is assigned to the asymmetric stretching mode of CH_2 bonds [60], while that at 3020 cm^{-1} is due to C–H bonds observed in aromatic rings [61]. The broad band centered at about 3300 cm^{-1} has been attributed to hydroxyl and amine groups present in the silica structure [56,62].

It can be observed from Figure 1 that the absorption band at 960 cm^{-1} was more visible for pure silica than for the amine-loaded samples. This result reveals that Si-OH groups were consumed as amino groups were incorporated into the silica matrix by the grafting approach [63]. Indeed, silanol groups have been reported to have an improved affinity for amine groups, which allows the chemical modification of silica with the latter groups [64]. In the case of the materials resulting from the co-condensation method, the amine groups do not participate in the polycondensation reactions leading to the 3D mesoporous network, and many of them could stay on the surface of the material instead of the silanol groups. The appearance of bands ascribed to APTES (2870 cm^{-1} and 2930 cm^{-1}) in the spectra of amino-loaded materials reveals that such groups were successfully incorporated into the silica structure. Nonetheless, these absorption bands

were more visible for samples prepared by co-condensation than for amine-grafted materials. Figure 2 displays typical thermograms obtained in this study. It can be observed that the amine-loaded sample prepared by co-condensation showed the highest mass loss (over 30 %), followed by the material obtained by grafting (≈ 17 %) and pure silica (≈ 11 %). Based on the mass loss observed in the temperature range of 390-650 °C and Equation (1), the concentration of amino groups in the functionalized samples was evaluated. We observed that specimens prepared by co-condensation displayed a higher concentration of amino groups than the grafted ones. For instance, MESO C_Co and SBA-16_Co exhibited a concentration of amine groups around 2.1 mmol.g^{-1} and 2.3 mmol.g^{-1}, while MESO C_Gra and SBA-16_ Gra showed loadings of about 1.0 mmol.g^{-1} and 1.4 mmol.g^{-1}.

Figure 3a depicts N_2 sorption isotherms obtained in this study. According to IUPAC [65], these isotherms have been classified as type IV and are commonly associated with mesoporous solids. A hysteresis loop attributed to the capillary condensation of N_2 in mesopores is observed for SBA-16. However, it is less noticeable for MESO A, MESO B, and MESO C. This result reveals that SBA-16 has a higher volume of mesopores than the other silica matrices prepared here. As observed in Figure S2, SBA-16_Co and SBA-16_Gra showed a narrower hysteresis loop and a lower N_2 adsorption capacity than SBA-16: 115 $cm^3.g^{-1}$, 164 $cm^3.g^{-1}$, and 356 $cm^3.g^{-1}$ for SBA-16_Co, SBA-16_Gra, and SBA-16, respectively. This behavior could be related to the partial blockage of the silica pore network as amino groups were incorporated into its structure. A similar trend was observed for MESO C because this sample exhibited a type IV isotherm, while MESO C_Co showed a type III isotherm related to macroporous materials (not shown here) [65].

Table 2 provides the textural properties obtained by N_2 sorption. The pure silica samples have mesoporous structures and ϕ between (2.3 ± 0.2) nm and (3.3 ± 0.2) nm. According to IUPAC, mesoporous solids have mean pore sizes ranging from 2 to 50 nm [65]. Besides, these materials showed SSA ranging from (561 ± 28) $m^2.g^{-1}$ to (705 ± 35) $m^2.g^{-1}$ and V_{mes} as large as (55 ± 3) × 10^{-2} $cm^3.g^{-1}$. As mentioned before, the hysteresis loops observed in Figure 3 are due to the capillary condensation of N_2 in mesopores. The grafting method caused a dramatic decrease in SSA and V_{mes} for the pure silica matrices, which seems to be related to the reduction in the surface area available for N_2 adsorption due to the presence of amine groups. Moreover, the presence of these chemical groups caused a slight increase in the mean pore size (ϕ), which could result from the blocking of small pores during the grafting process. Samples obtained by the co-condensation of TEOS and APTES exhibited a smaller SSA and higher V_{mes} than the corresponding pure specimens. Moreover, they also displayed a larger ϕ. Nonetheless, this behavior was not observed for SBA-16_Co, which showed a smaller V_{mes} than SBA-16. It is worth stressing that the co-condensation process has its own hydrolysis and condensation mechanisms, which could lead to samples with pore structures different from those observed for the pure silica matrices.

The grafting route used in this work consisted of soaking the previously-prepared silica samples in a solution of APTES and Tol. The excess of APTES was subsequently removed by vacuum filtration with EtOH and Tol. The removal of APTES is an essential step because its presence could block the pore structure of silica, negatively affecting its adsorption properties. In this case, amino groups are expected to be present on the surface and in the pore walls of silica. On the other hand, the co-condensation of

TEOS and APTES allows incorporating amino groups within the silica framework and not only on its surface and pore walls. As a consequence, materials derived from this chemical route should have amino groups immobilized within the silica structure in addition to those observed in the pore structure [66]. This behavior could justify the higher concentration of amino groups in samples prepared by co-condensation than the amine-grafted specimens. Moreover, the presence of amino groups at more significant loadings in these samples could also be related to their smaller SSA when compared to pure silica specimens (Table 2). Nonetheless, these materials displayed a larger V_{mes} and ϕ than the latter. It has been reported that APTES show fast hydrolysis reactions due to the existence of amino groups in their structure [51]. Besides, such groups also affect the co-condensation process due to their strong interaction with the silicate species formed during the sol-gel step [67]. Therefore, it is reasonable to expect that the specimens prepared by the co-condensation of TEOS and APTES have different pore structures from those observed for pure silica.

Figure 4 shows the Zeta potential curves collected for pure and amine-containing samples. Pure silica displayed an isoelectric point (IEP) around pH 3.4. The IEP of silica is reported to be between pH 2.0 and 3.0 [68], which is consistent with the result obtained here. Silica becomes protonated and deprotonated at pH below and above IEP as schematically shown in Equations (5) and (6) [69], justifying its positive or negative surface charges under these conditions.

$$\equiv \mathrm{SiOH} + \mathrm{H_3O^+} \rightleftharpoons \mathrm{Si - OH_2^+} + \mathrm{H_2O} \quad (5)$$

$$\equiv \mathrm{SiOH} + \mathrm{OH^-} \rightleftharpoons \mathrm{Si{-}O^-} + \mathrm{H_2O} \quad (6)$$

The addition of amino groups shifted the IEP of silica towards higher pH; amine-containing materials prepared by grafting and co-condensation exhibited an IEP around 6.0 and 8.0, respectively. As displayed in Figure 2, samples derived from the co-condensation route had a higher concentration of amino groups than the grafted ones. It can be suggested that the positively charged amino groups bonded to silica counteract its negative hydroxyl terminations, causing the observed change in IEP. Similar behavior was also reported elsewhere [70,71]. For pH above IEP, such amino groups are deprotonated, leading to negative Zeta potentials.

Figure 5 displays SEM micrographs taken in this study. SBA-16 has a broad particle size distribution and a porous appearance; this sample shows particles with sizes below 50 μm and above 400 μm. Besides, pores as large as 20 μm are observed in this material. MESO C also has wide size distribution and particles with irregular shapes. However, no evident change in particle size and morphology was observed after the grafting step (MESO C_Gra). It is worth noticing that the MESO C-related materials (pure and amino-containing samples) were ground in an agate mortar after their preparation, justifying their wide particle size distribution and irregular shape. However, the co-condensation of TEOS and APTES had a significant effect on these properties; one observes that MESO C_Co has a smaller particle size distribution than the other samples, in addition to particles with a distinct shape. This effect can be related to the occurrence of rapid hydrolysis and condensation reactions when APTES was added to the starting sol-gel solution, leading to macroporous structures as observed by N_2 sorption (Figure 3 and Table 2). Such structures could easily crack during the drying step and gave rise to finer particles.

3.2 ADSORPTION TESTS

- MB

Figure 6 shows the adsorption curves obtained for the pure silica matrices. The pH of the MB solution containing the pure silica matrices stabilized at about 4.5. On the other hand, the addition of amine-loaded samples caused this pH to shift to about 7.5. This behavior could be due to the pKa of the silanol groups present on the silica surface, and APTES used to obtain the amine-loaded samples; the pKa of silanol groups and APTES have been reported to be about 5.6 and 10.6, respectively. As will be discussed in detail later, at a pH below or above the pKa, a chemical species tend to be protonated or deprotonated. Thus, the addition of silica into the MB solution initially present at pH 7.0 causes the deprotonation of silanol groups, shifting the pH of the solution to 4.5. In contrast, APTES becomes protonated at pH 7.0 and shifts the pH of the solution to 7.5 [72].

One observes from Figure 6 that MESO C exhibited the highest adsorption capacity (≈ 26 $mg.g^{-1}$), followed by SBA-16 (≈ 24 $mg.g^{-1}$), MESO A (≈ 21 $mg.g^{-1}$), and MESO B (≈ 18 $mg.g^{-1}$). The solid lines were calculated by applying the Lagergren kinetic model to the experimental curves. This empirical model has been used to study a range of materials [45,73–75]. The pseudo-n^{th}-order kinetic law of Lagergren is expressed by Equation (7), where k_n represents the rate constant for the n^{th}-order adsorption (min^{-1}), q_e is the uptake capacity at equilibrium ($mg.g^{-1}$), and q_t is the adsorption capacity at a time t ($mg.g^{-1}$) [76].

$$\frac{dq_t}{dt} = k_n(q_e - q_t)^n \quad (7)$$

The integration of Equation (7) between t = 0 and t = t (q_0 = 0 and $q_t = q_t$) leads to Equations (8) and (9) for the pseudo-first (n = 1) and pseudo-second-order (n = 2) laws, respectively.

$$q_t = q_e(1 - \exp(-k_1 t)) \quad (8)$$

$$q_t = \frac{k_2 q_e^2 t}{1 + k_2 q_e t} \quad (9)$$

Equations (8) and (9) can be linearized, as expressed in Equations (10) and (11).

$$\ln(q_e - q_t) = \ln(q_e) - k_1 t \quad (10)$$

$$\frac{1}{q_e - q_t} = \frac{1}{q_e} + k_2 t \quad (11)$$

Therefore, k_1 and k_2 can be evaluated by assessing $\ln(q_e - q_t)$ and $1/(q_e - q_t)$ as a function of time. Table 3 provides the kinetic parameters evaluated after performing these calculations. One observes that the pseudo-second-order law fitted well to the experimental curves since the values obtained for R^2 (goodness-of-fit) were above 0.9. This finding justifies why the solid lines exhibited in Figure 6 are close to the experimental data points. On the other hand, the pseudo-first-order kinetic model did not fit well with the experimental data and was not considered. It is worth mentioning

that the solid lines drawn in Figure 6 were obtained after performing the least square fitting method on the experimental data points.

One notices from Figure 6 and Table 3 that both MESO C and SBA-16 displayed a slow adsorption rate (4×10^{-4} min^{-1}) and a high adsorption capacity (25.5 $mg.g^{-1}$ and 24.2 $mg.g^{-1}$, respectively). MESO A exhibited an intermediary adsorption rate (11×10^{-4} min^{-1}) and uptake capacity (20.9 $mg.g^{-1}$). MESO B was the pure sample with the fastest adsorption rate (59×10^{-4} min^{-1}) and the smallest adsorption capacity (17.9 $mg.g^{-1}$). It can be observed from Table 2 that MESO C and SBA-16 were the silica matrices with the largest SSA (705 ± 35 $m^2.g^{-1}$ and 677 ± 34 $m^2.g^{-1}$) and V_{mes} ($(41 \pm 2) \times 10^{-2}$ $cm^3.g^{-1}$ and $(55 \pm 3) \times 10^{-2}$ $cm^3.g^{-1}$), which can contribute to the improved adsorption capacity exhibited by these materials. However, such SSA and V_{mes} demand longer times to reach the adsorption equilibrium, justifying the low adsorption rate of MESO C and SBA-16. This behavior is especially true for the specimens prepared in this study due to their relatively small pore size in the range of 2-3 nm, which is only twice as large as MB molecules (≈ 1.4 nm) [77]. These properties make the diffusion of MB molecules into the pore structure of silica a time-consuming process.

Figure 7 depicts the adsorption curves evaluated for MESO C and SBA-16 before and after modification with amino groups using the post-grafting and co-condensation methods. These silica matrices were chosen to be chemically modified with amino groups because they had the most promising adsorption behavior (Figure 6 and Table 3). MESO C_Gra displayed a higher adsorption capacity than MESO C and MESO C_CO: 28.8 $mg.g^{-1}$ versus 25.5 $mg.g^{-1}$ and 2.0 $mg.g^{-1}$, respectively. On the other hand, the incorporation of amino groups into SBA-16 decreased its adsorption capacity from

24.2 $mg.g^{-1}$ to 6.2 $mg.g^{-1}$ (SBA-16_Gra) and 9.4 $mg.g^{-1}$ (SBA-16_Co). As shown in Table 2, SBA-16 experienced a significant decrease in SSA and V_{mes} after the grafting step: 64 % and 55 %, respectively. MESO C also displayed a decrease in these properties after grafting, but it was smaller: 52 % for SSA and 46 % for V_{mes}.

The incorporation of amino groups into the silica framework by co-condensation was detrimental to the adsorption properties of MESO C and SBA-16. MESO C_Co and SBA-16_Co exhibited SSA of about (99 ± 5) $m^2.g^{-1}$ and (198 ± 10) $m^2.g^{-1}$. These values are significantly smaller than those evaluated for MESO C and SBA-16 (Table 2). Regarding SBA-16_Co, it is also worth noting that it was prepared using a molar ratio of (TEOS + APTES): H_2O of 1: 147, while MESO C_Co is derived from a solution with a lower concentration of water (0.9 TEOS: 0.1 APTES: 20 H_2O). Consequently, the lack of H_2O in the solution used to prepare MESO C_Co led to a denser material, showing a smaller area available for adsorption. MESO C_Co and SBA-16_Co displayed adsorption capacities of about 2.0 $mg.g^{-1}$ and 9.4 $mg.g^{-1}$, respectively. It is also worth considering that the pH of the MB solution after the addition of amine-loaded samples stabilized at around 7.5. As observed in Figure 4, at this pH, the Zeta potential of co-condensation-derived samples was positive, which could inhibit the adsorption of MB molecules by these materials since MB is also positively charged at pH 7.5 [78].

Changes in the pH of a solution can greatly impact the adsorption behavior of a sorbent. By evaluating its adsorption capacity at different pH, it is possible to determine the optimum conditions for using a sorbent. The silica matrices that exhibited the best performances in the previous tests (Figures 6 and 7) were examined using MB solutions at different pH. Figure 8 exhibits the adsorption curves of MESO C and SBA-16 using

solutions with pH ranging from 3.0 to 9.0. One observes that both samples experienced a noticeable increase in the adsorption capacity when the pH of the solution was increased from 3.0 to 4.5, 7.0, or 9.0. MESO C displayed the following adsorption capacities at pH = 3.0, 4.5, 7.0, and 9.0: 10.2 $mg.g^{-1}$, 25.5 $mg.g^{-1}$, 36.9 $mg.g^{-1}$, and 37.2 $mg.g^{-1}$, respectively. On the other hand, SBA-16 showed the following adsorption capacities: 19.7 $mg.g^{-1}$ (pH = 3.0), 24.2 $mg.g^{-1}$ (pH = 4.5), 37.4 $mg.g^{-1}$ (pH = 7.0), and 37.1 $mg.g^{-1}$ (pH = 9.0). Moreover, the adsorption kinetics was greatly accelerated with increasing the pH of the solution; according to the pseudo-second-order kinetic model described in Equation (11), the adsorption rates of MESO C and SBA-16 at pH = 9.0 were as high as 1.5×10^{-2} min^{-1} and 1.0×10^{-1} min^{-1}, respectively.

Since MB is cationic, the driving force to adsorb it is greater for negatively charged surfaces. Such a scenario is observed for pH above the IEP of silica due to its deprotonation, which was evaluated in this work to be about pH 3.4. Consequently, at pH = 4.5, 7.0, or 9.0, the silica surface is negatively charged, favoring the adsorption of MB molecules. At pH = 7.0 and 9.0, the negative charge on the silica surface is so high that MESO C and SBA-16 showed fast and high adsorption; it is important noting that the adsorption behavior of these specimens was similar at pH = 7.0 or 9.0. Figure 9 shows the adsorption curves taken for MESO C_Gra and MESO C_Co at different pH. As observed in Figure 4, the incorporation of amino groups into silica has changed its IEP towards larger pH; amine-containing materials prepared by grafting and co-condensation showed IEPs around 6.0 and 8.0, respectively. This behavior justifies the low adsorption capacity of MESO C_Co: its surface is positively charged at pH below 8.0 and slightly negative at pH above this value. This is why the driving force to adsorb MB is weak even at a pH as high as 9.0, justifying the low adsorption capacity of

MESO C_Co. At pH = 3.0, 4.5, and 9.0 the adsorption capacities of MESO C_Co and MESO C_Gra were: 3.5 $mg.g^{-1}$ and 3.2 $mg.g^{-1}$, 1.8 $mg.g^{-1}$ and 28.8 $mg.g^{-1}$, and 10.7 $mg.g^{-1}$ and 34.4 $mg.g^{-1}$.

The chemical modification of MESO C with amino groups by the grafting route enhanced its adsorption capacity (MESO C_Gra). Such a behavior can be due to the synergistic effect between the pore structure of this material and the presence of amine groups, which have a strong affinity for MB. At this point, it is important to note that MESO C was prepared following a simple procedure where no acidic or basic catalyst, templating agent, or heat treatment was used. On the other hand, SBA-16 was obtained after using HCl as a catalyst and Pluronic® F127 as a template. Besides, a heat treatment step at 500 °C for 6 h in air was applied to remove F127® from the silica network and allow the fabrication of samples with an open and ordered mesoporous structure. The absence of such steps in the preparation of MESO C may represent a significant advantage in terms of energy and time savings. Moreover, it is a facile route.

Pernyeszi *et al.* [79] investigated the adsorption process of MB on microcline particles. They reported that the maximum adsorption capacities were in the range of 1.5-3.1 $mg.g^{-1}$. Bulut and Aydın [80] described an adsorption capacity of 9.6 $mg.g^{-1}$ on wheat shells, while Kannan and Sundaram [81] reported uptake capacities ranging from about 10.0 $mg.g^{-1}$ to 20.0 $mg.g^{-1}$ for carbon samples derived from different sources, including bamboo dust, coconut shell, and rice rusk. Tehrani-Bagha *et al.* [82] and Hassani *et al.* [83] reported a maximum uptake capacity of about 30.0 $mg.g^{-1}$ and 31.4 $mg.g^{-1}$ for kaolin and Turkish lignite samples. Pan *et al.* [84] described an adsorption capacity of around 36.8 $mg.g^{-1}$ for adsorption tests conducted at room temperature using

self-assembled three-dimensional MgAl layered double hydroxides. This behavior reinforces that the silica samples prepared here have adsorption capacity similar to other materials already reported in the literature. Nonetheless, it is important to mention that such a comparison is not always straightforward due to the varying adsorption conditions used by different authors, including the adsorbent loading, pollutant concentration, pH of the solution tested, and adsorption temperature.

- DIP

Figure 10 displays the adsorption curves obtained for DIP at pH = 3.0, 7.0, or 9.0. One observes that MESO C showed its highest adsorption capacity at pH 7.0. DIP has been reported to have a pKa at about 4.0 [41,85]. The Henderson-Hasselbalch equation [86] establishes a relationship between pH and pKa as demonstrated in Equation (12), where $[A^-]$ and [HA] are the concentrations of the deprotonated and protonated forms of an acidic species.

$$\mathrm{pH} = \mathrm{pKa} + \log\frac{[A^-]}{[\mathrm{HA}]} \quad (12)$$

According to Equation (12), at pH = 4.0, 50 % of the sulfite groups present in DIP are deprotonated, while 50 % are protonated. Thus, at pH above 4.0, many functional groups of DIP are deprotonated, revealing that the drug molecules have a negatively charged surface. As mentioned before, the IEP of silica is reached when the pH of the medium is about 3.0, revealing that it shows no surface electric charge at this condition. The lack of surface charges on silica and the neutral character of DIP at this pH could have inhibited the adsorption of the latter. On the other hand, at pH = 9.0, the adsorption

process could be disfavored due to the excessive deprotonation of DIP sulfite groups [87,88], leading to a large concentration of molecules in the anionic form and improving the electrostatic repulsion between the negatively charged sites on the silica surface and drug molecules. MESO C has an adsorption capacity of 8.2 $mg.g^{-1}$ at pH = 7.0, revealing that this pH should be taken as a reference when preparing this sample for adsorption or drug delivery purposes. MESO C_Gra, on the other hand, displayed a higher uptake capacity at pH = 9.0 (6.0 $mg.g^{-1}$) than at pH = 7.0 (3.7 $mg.g^{-1}$), despite the slower adsorption in the former condition (3.4×10^{-4} versus 3.7×10^{-3} min^{-1}). This result can be related to the distinct IEP of MESO C and MESO C_Gra and the presence of amino groups in the latter, which significantly affects its interfacial behavior. Moreover, we should consider that these functional groups have a strong affinity for DIP. MESO C_Gra had negligible adsorption at pH = 3.0, and this adsorption curve is not shown in Figure 10.

The incorporation of DIP into silica is commonly reported in the literature to investigate the use of these materials in drug delivery systems. Consequently, silica is usually soaked in highly concentrated DIP solutions (in the order of tens $g.L^{-1}$) to improve the loading of this pharmaceutical in the silica structure. We investigated in this work the adsorption of DIP using solutions with much lower concentrations (0.1 $g.L^{-1}$). Andrade *et al.* [89] studied the adsorption of DIP on graphene oxide sheets decorated with Fe_2O_3/ZnO nanoparticles. The authors reported a maximum adsorption capacity of 15.2 $mg.g^{-1}$ at 45 °C and pH = 5.8 when the pollutant concentration was 0.01 $g.L^{-1}$. Carvalho *et al.* [42] applied chitosan microspheres in the removal of diclofenac and DIP from water. They performed an in-depth investigation of the thermodynamic aspects involved in the adsorption process. The adsorption capacity of the chitosan samples

prepared was reported to be 16.1 $mg.g^{-1}$. Springer *et al.* [90] investigated the adsorption behavior of magnetic nickel ferrite nanoparticles with sizes around 20 nm. They reported uptake capacities as high as 30.4 $mg.g^{-1}$ at pH = 6. Despite the higher adsorption capacity reported in these works, we reinforce that the synthesis procedures used here are more straightforward, which increases their applicability.

- COMPARISON BETWEEN MB AND DIP

As already discussed, MESO C was the best sample in terms of MB and DIP adsorption. The adsorption values evaluated at pH 7.0 were 36.9 $mg.g^{-1}$ (MB) and 8.2 $mg.g^{-1}$ (DIP). The molecular weights of MB and DIP are 333.34 $g.mol^{-1}$ and 319.85 $g.mol^{-1}$, respectively. By considering these molecular weights, one can show that the adsorption capacities of MESO C at pH 7.0 are about 111 $\mu mol.g^{-1}$ (MB) and 25 $\mu mol.g^{-1}$ (DIP). This difference could be related to the distinct molecular structures and chemical behavior of these pollutants. Despite the lower capacity to adsorb DIP exhibited by the samples prepared here, such materials could be used to remove this pollutant from aqueous media. We will investigate the release of DIP from these samples when dispersed in simulated body fluid for application in drug delivery systems in future work. We intentionally used pollutants with different behaviors in this work to evaluate the versatility of the prepared adsorbents. Such an approach is barely observed in the literature.

Different mechanisms have been reported in the literature for the adsorption of organic pollutants on the silica surface. The first mechanism is associated with the electrostatic interaction between the silica surface and organic molecules. Such a mechanism is

strongly related to the pH and pKa of the solution and the pollutant. As shown in Equation (12), the presence of protonated or deprotonated groups and, consequently, the surface charge of silica and the pollutant molecules depends on the pH of the solution. The significant concentration of silanol groups on the surface of the silica samples prepared here (Figure 1) favors the adsorption of MB and DIP on them. Moreover, the higher the pH of the solution, the more protonated these groups are, which enhances the electrostatic interaction between the silica surface and these pollutants (Figure 8). The second mechanism, also known as dipole-dipole hydrogen bonding, is ascribed to hydrogen bonds derived from the interaction between hydroxyl groups (H-donors) present on the silica surface and nitrogen atoms (H-acceptors) observed in MB and DIP. The third mechanism is the so-called n-π interactions and is derived from the interaction between electron donor and electron acceptor atoms. Atoms such as the oxygen observed on the silica surface or the nitrogen from APTES can play an electron donor role, while the aromatic rings from MB and DIP can act as electron acceptors [91]. We believe that all of these mechanisms could contribute to the adsorption of MB and DIP on the samples prepared here. The presence of amine groups on the silica surface contributed to the occurrence of n-π interactions, increasing the affinity of the amine-loaded samples for the tested pollutants.

- REGENERATION TESTS

Aiming to investigate the thermal regeneration of the silica-based sorbents prepared in this work, we conducted the heat-treatment of these materials after the adsorption tests. Thus, the used adsorbents were heat-treated at 450 °C for 15 min in air. Previous tests revealed that it was not possible to regenerate these adsorbents when using temperatures

below 450 °C fully. Thus, the heat treatment was kept as short as possible to inhibit the change of the silica pore network during this step. Figure 11 displays the removal efficiency evaluated for MESO C after four adsorption-desorption cycles. The efficiency of this sample changed from 94.0 % to 92.3 % for MB and from 21.0 % to 19.4% for DIP. This result reveals that the adsorbents prepared here can be easily regenerated after an adsorption step by heat treatment at 450 °C for periods as short as 15 min. The use of a short regeneration time is a strategic advantage in terms of energy and time savings. In the case of regenerating amine-loaded sorbents, it would be important to keep the heat treatment time as short as possible to mitigate the removal of such functional groups from them. However, it is worth recalling that although the amine groups begin to be removed from the silica at 390 °C, this process is only completed at temperatures as high as 650 °C (Figure 2). Thus, we believe that amine-loaded samples could also be treated at 450 °C for periods as short as 15 min without a significant decrease in their adsorption capacity.

4. CONCLUSIONS

Silica-based adsorbents were prepared in this work by a facile synthesis route where no catalysts, surfactants, or heat treatment steps were used. Such materials have a mesoporous pore network and SSAs as high as (705 ± 35) $m^2.g^{-1}$. Amino groups were incorporated into these samples to investigate the influence of these chemical groups on their adsorption behavior. The co-condensation of TEOS and ATPES led to specimens with amine loadings higher than the materials derived from a grafting approach. The presence of amino groups in silica has changed its IEP from about pH = 3.4 to 6.0 or 8.0, which had a significant effect on the adsorption behavior of the prepared

adsorbents. MESO C, which was prepared using a molar ratio of 1 TEOS: 4 APTES: 20 H_2O, was the silica matrix with the highest MB adsorption capacity at pH 4.5. However, changing the pH of the MB solution had a significant effect on its adsorption behavior; at pH = 3.0, 4.5, 7.0, and 9.0 the adsorption capacities evaluated for MESO C were 10.2 $mg.g^{-1}$, 25.5 $mg.g^{-1}$, 36.9 $mg.g^{-1}$, and 37.2 $mg.g^{-1}$, respectively. These values correspond to removal efficiencies of 25.5 %, 63.8 %, 92.3 %, and 93.0 %. This material also displayed a promising capacity for adsorbing DIP, reaching an adsorption capacity of 8.2 $mg.g^{-1}$ (20.5 %) at pH = 7.0. Finally, we successfully regenerated this sample after a heat treatment at 450 °C for 15 min, which allows it to be used in successive adsorption cycles. The short time needed to regenerate these materials represents a key advantage in terms of energy and time savings.

ACKNOWLEDGMENTS

The authors thank the financial support from CNPq (301423/2018-0 and 306193/2020), CAPES (PROEX), and FAPEMIG (APQ-00792-17 and RED-00102-16). We also thank the UFMG Microscopy Center, LEPCom (Prof. Rodrigo Oréfice), CeNano^{2}I/CEMUCASI (Prof. Herman Mansur and Dr. Alexandra Mansur), and PUC-MG (prof. Leonardo Mitre) for the technical support of this research.

REFERENCES

[1] Van Boeckel TP, Gandra S, Ashok A, Caudron Q, Grenfell BT, Levin SA, et al. Global antibiotic consumption 2000 to 2010: An analysis of national pharmaceutical sales data. Lancet Infect Dis 2014;14:742–50.

https://doi.org/10.1016/S1473-3099(14)70780-7.

[2] Quadra GR, Silva PSA, Paranaíba JR, Josué IIP, Souza H, Costa R, et al. Investigation of medicines consumption and disposal in Brazil: A study case in a developing country. Sci Total Environ 2019;671:505–9. https://doi.org/10.1016/j.scitotenv.2019.03.334.

[3] Vellinga A, Cormican S, Driscoll J, Furey M, O'Sullivan M, Cormican M. Public practice regarding disposal of unused medicines in Ireland. Sci Total Environ 2014;478:98–102. https://doi.org/10.1016/j.scitotenv.2014.01.085.

[4] Cerrato G, Bianchi CL, Galli F, Pirola C, Morandi S, Capucci V. Micro-TiO_2 coated glass surfaces safely abate drugs in surface water. J Hazard Mater 2019;363:328–34. https://doi.org/10.1016/j.jhazmat.2018.09.057.

[5] aus der Beek T, Weber FA, Bergmann A, Hickmann S, Ebert I, Hein A, et al. Pharmaceuticals in the environment-Global occurrences and perspectives. Environ Toxicol Chem 2016;35:823–35. https://doi.org/10.1002/etc.3339.

[6] Weigmann K. Swimming in a sea of drugs. EMBO Rep 2017;18:1688–92. https://doi.org/10.15252/embr.201745015.

[7] Gunnarsson L, Snape JR, Verbruggen B, Owen SF, Kristiansson E, Margiotta-Casaluci L, et al. Pharmacology beyond the patient – The environmental risks of human drugs. Environ Int 2019;129:320–32. https://doi.org/10.1016/j.envint.2019.04.075.

[8] Kasonga TK, Coetzee MAA, Kamika I, Ngole-Jeme VM, Benteke Momba MN. Endocrine-disruptive chemicals as contaminants of emerging concern in wastewater and surface water: A review. J Environ Manage 2021;277:111485.

https://doi.org/10.1016/j.jenvman.2020.111485.

[9] González Peña OI, López Zavala MÁ, Cabral Ruelas H. Pharmaceuticals market, consumption trends and disease incidence are not driving the pharmaceutical research on water and wastewater. Int J Environ Res Public Health 2021;18. https://doi.org/10.3390/ijerph18052532.

[10] Tang H, Wang J, Zhang S, Pang H, Wang X, Chen Z, et al. Recent advances in nanoscale zero-valent iron-based materials: Characteristics, environmental remediation and challenges. J Clean Prod 2021;319:128641. https://doi.org/10.1016/j.jclepro.2021.128641.

[11] Magdy YH, Altaher H. Kinetic analysis of the adsorption of dyes from high strength wastewater on cement kiln dust. J Environ Chem Eng 2018;6:834–41. https://doi.org/10.1016/j.jece.2018.01.009.

[12] Vacchi FI, Von der Ohe PC, Albuquerque AF de, Vendemiatti JA de S, Azevedo CCJ, Honório JG, et al. Occurrence and risk assessment of an azo dye - The case of Disperse Red 1. Chemosphere 2016;156:95–100. https://doi.org/10.1016/j.chemosphere.2016.04.121.

[13] Chan SHS, Wu TY, Juan JC, Teh CY. Recent developments of metal oxide semiconductors as photocatalysts in advanced oxidation processes (AOPs) for treatment of dye waste-water. J Chem Technol Biotechnol 2011;86:1130–58. https://doi.org/10.1002/jctb.2636.

[14] Sen TK, Afroze S, Ang HM. Equilibrium, kinetics and mechanism of removal of methylene blue from aqueous solution by adsorption onto pine cone biomass of Pinus radiata. Water Air Soil Pollut 2011;218:499–515.

https://doi.org/10.1007/s11270-010-0663-y.

[15] JianLong W, Hai C. Catalytic ozonation for water and wastewater treatment: recent advances and perspective. Sci Total Environ 2020;704:135249. https://doi.org/10.1016/j.scitotenv.2019.135249.

[16] Martínez-Huitle CA, Panizza M. Electrochemical oxidation of organic pollutants for wastewater treatment. Curr Opin Electrochem 2018;11:62–71. https://doi.org/10.1016/j.coelec.2018.07.010.

[17] Gonçalves BS, Souza TCC de, Castro VG de, Silva GG, Houmard M, Nunes EHM. Solvent effect on the structure and photocatalytic behavior of TiO_2-RGO nanocomposites. J Mater Res 2019;34:3918–30. https://doi.org/10.1557/jmr.2019.342.

[18] Gonçalves BS, Palhares HG, de Souza TCC, de Castro VG, Silva GG, Houmard M, et al. Effect of the carbon loading on the structural and photocatalytic properties of reduced graphene oxide-TiO_2 nanocomposites prepared by hydrothermal synthesis. J Mater Res Technol 2019;8:6262–74. https://doi.org/10.1016/j.jmrt.2019.10.020.

[19] Palhares HG, Gonçalves BS, Silva LMC, Nunes EHM, Houmard M. Clarifying the roles of hydrothermal treatment and silica addition to synthesize TiO_2-based nanocomposites with high photocatalytic performance. J Sol-Gel Sci Technol 2020;95:119–35. https://doi.org/10.1007/s10971-020-05265-4.

[20] Alahmadi N, Amin MS, Mohamed RM. Facile synthesis of mesoporous Pt-doped, titania-silica nanocomposites as highly photoactive under visible light. J Mater Res Technol 2020;9:14093–102.

https://doi.org/10.1016/j.jmrt.2020.10.004.

[21] Mirsadeghi S, Zandavar H, Rajabi HR, Sajadiasl F, Ganjali MR, Pourmortazavi SM. Superior degradation of organic pollutants and H_2O_2 generation ability on environmentally-sound constructed Fe3O4-Cu nanocomposite. J Mater Res Technol 2021;14:808–21. https://doi.org/10.1016/j.jmrt.2021.07.007.

[22] Said B, M'rabet S, Hsissou R, Harfi A El. Synthesis of new low-cost organic ultrafiltration membrane made from Polysulfone/Polyetherimide blends and its application for soluble azoic dyes removal. J Mater Res Technol 2020;9:4763–72. https://doi.org/10.1016/j.jmrt.2020.02.102.

[23] Xu Y, Huang H, Ying G, Zhang J, Wu Y, Wu S, et al. Flexible, fouling-resistant and self-cleaning $Ti_3C_2T_x$-derivated hydrophilic nanofiltration membrane for highly efficient rejection of organic molecules from wastewater. J Mater Res Technol 2020;9:11675–86. https://doi.org/10.1016/j.jmrt.2020.08.031.

[24] Abdelrahman EA, Hegazey RM, El-Azabawy RE. Efficient removal of methylene blue dye from aqueous media using Fe/Si, Cr/Si, Ni/Si, and Zn/Si amorphous novel adsorbents. J Mater Res Technol 2019;8:5301–13. https://doi.org/10.1016/j.jmrt.2019.08.051.

[25] Liu X-J, Li M-F, Singh SK. Manganese-modified lignin biochar as adsorbent for removal of methylene blue. J Mater Res Technol 2021;12:1434–45. https://doi.org/10.1016/j.jmrt.2021.03.076.

[26] Wang J, Zhao S qi, Zhang M ya, He B shu. Targeted eco-pharmacovigilance for ketoprofen in the environment: Need, strategy and challenge. Chemosphere 2018;194:450–62. https://doi.org/10.1016/j.chemosphere.2017.12.020.

[27] Liu Y, Huo Y, Wang X, Yu S, Ai Y, Chen Z, et al. Impact of metal ions and organic ligands on uranium removal properties by zeolitic imidazolate framework materials. J Clean Prod 2021;278:123216. https://doi.org/10.1016/j.jclepro.2020.123216.

[28] Liu Y, Pang H, Wang X, Yu S, Chen Z, Zhang P, et al. Zeolitic imidazolate framework-based nanomaterials for the capture of heavy metal ions and radionuclides: A review. Chem Eng J 2021;406:127139. https://doi.org/10.1016/j.cej.2020.127139.

[29] Zheng J, Zhang M, Miao T, Yang J, Xu J, Alharbi NS, et al. Anchoring nickel nanoparticles on three-dimensionally macro-/mesoporous titanium dioxide with a carbon layer from polydopamine using polymethylmethacrylate microspheres as sacrificial templates. Mater Chem Front 2019;3:224–32.

[30] Zhang M, Ling Y, Liu L, Xu J, Li J, Fang Q. Carbon supported PdNi alloy nanoparticles on SiO_2 nanocages with enhanced catalytic performance. Inorg Chem Front 2020;7:3081–91. https://doi.org/10.1039/D0QI00596G.

[31] Wang WC, Zhou B, Xu SH, Yang ZM, Zhang QY. Recent advances in soft optical glass fiber and fiber lasers. Prog Mater Sci 2019;101:90–171. https://doi.org/10.1016/j.pmatsci.2018.11.003.

[32] Pyo Y, Robertson T, Yun S, Hong Z. Experimental evaluation of using silica aerogels as the thermal insulator for combustor liners. J Glob Power Propuls Soc 2020;4:202–16. https://doi.org/10.33737/jgpps/129703.

[33] Shafqat SS, Khan AA, Zafar MN, Alhaji MH, Sanaullah K, Shafqat SR, et al. Development of amino-functionalized silica nanoparticles for efficient and rapid

removal of COD from pre-treated palm oil effluent. J Mater Res Technol 2019;8:385–95. https://doi.org/10.1016/j.jmrt.2018.03.002.

[34] da Costa Farias RM, Mota MF, Severo LL, de Medeiros ES, Klamczynski AP, de Jesús Avena-Bustillos R, et al. Green synthesis of porous N-Carbon/Silica nanofibers by solution blow spinning and evaluation of their efficiency in dye adsorption. J Mater Res Technol 2020;9:3038–46. https://doi.org/10.1016/j.jmrt.2020.01.034.

[35] Diosa J, Poveda-Jaramillo JC, Ramirez-Rodríguez F, Mesa M. Modeling surface chemistry and adsorption behavior of biomimetic chitosan/silica hybrid materials. J Mater Res Technol 2020;9:8092–103. https://doi.org/10.1016/j.jmrt.2020.05.100.

[36] Schubert U. Chemistry and fundamentals of the sol-gel process. Sol-Gel Handb., John Wiley & Sons, Ltd; 2015, p. 1–28. https://doi.org/10.1002/9783527670819.ch01.

[37] Senthilkumaar S, Varadarajan PR, Porkodi K, Subbhuraam C V. Adsorption of methylene blue onto jute fiber carbon: Kinetics and equilibrium studies. J Colloid Interface Sci 2005;284:78–82. https://doi.org/10.1016/j.jcis.2004.09.027.

[38] Shahabuddin S, Sarih NM, Kamboh MA, Nodeh HR, Mohamad S. Synthesis of polyaniline-coated graphene oxide@$SrTiO_3$ nanocube nanocomposites for enhanced removal of carcinogenic dyes from aqueous solution. Polymers (Basel) 2016;8:305. https://doi.org/10.3390/polym8090305.

[39] Marques BS, Frantz TS, Sant'Anna Cadaval Junior TR, de Almeida Pinto LA, Dotto GL. Adsorption of a textile dye onto piaçava fibers: kinetic, equilibrium,

thermodynamics, and application in simulated effluents. Environ Sci Pollut Res 2019;26:28584–92. https://doi.org/10.1007/s11356-018-3587-5.

[40] Ambalavanar V, Habekost A. The analgesic metamizol (dipyrone). Part 2: Adsorption, oxidative and reductive degradation. World J Chem Educ 2018;6:204–11. https://doi.org/10.12691/wjce-6-5-1.

[41] Licona KPM, O. Geaquinto LR de, Nicolini JV, Figueiredo NG, Chiapetta SC, Habert AC, et al. Assessing potential of nanofiltration and reverse osmosis for removal of toxic pharmaceuticals from water. J Water Process Eng 2018;25:195–204. https://doi.org/j.jwpe.2018.08.002.

[42] Carvalho TO, Matias AEB, Braga LR, Evangelista SM, Prado AGS. Calorimetric studies of removal of nonsteroidal anti-inflammatory drugs diclofenac and dipyrone from water. J. Therm. Anal. Calorim., vol. 106, 2011, p. 475–81. https://doi.org/10.1007/s10973-010-1243-5.

[43] Karim AH, Jalil AA, Triwahyono S, Sidik SM, Kamarudin NHN, Jusoh R, et al. Amino modified mesostructured silica nanoparticles for efficient adsorption of methylene blue. J Colloid Interface Sci 2012;386:307–14. https://doi.org/10.1016/j.jcis.2012.07.043.

[44] Houmard M, Nunes EHM, Vasconcelos DCL, Berthomé G, Joud JC, Langlet M, et al. Correlation between sol-gel reactivity and wettability of silica films deposited on stainless steel. Appl Surf Sci 2014;289:218–23. https://doi.org/10.1016/j.apsusc.2013.10.137.

[45] Mota TLR, Marques de Oliveira AP, Nunes EHM, Houmard M. Simple process for preparing mesoporous sol-gel silica adsorbents with high water adsorption

capacities. Microporous Mesoporous Mater 2017;253:177–82. https://doi.org/10.1016/j.micromeso.2017.07.010.

[46] Mota TLR, Gomes ALM, Palhares HG, Nunes EHM, Houmard M. Influence of the synthesis parameters on the mesoporous structure and adsorption behavior of silica xerogels fabricated by sol–gel technique. J Sol-Gel Sci Technol 2019;92:681–94. https://doi.org/10.1007/s10971-019-05131-y.

[47] Chaudhuri H, Dash S, Ghorai S, Pal S, Sarkar A. SBA-16: Application for the removal of neutral, cationic, and anionic dyes from aqueous medium. J Environ Chem Eng 2016;4:157–66. https://doi.org/10.1016/j.jece.2015.11.020.

[48] Akhtar J, Amin NAS, Shahzad K. A review on removal of pharmaceuticals from water by adsorption. Desalin Water Treat 2016;57:12842–60. https://doi.org/10.1080/19443994.2015.1051121.

[49] de O. N. Ribeiro J, Nunes EHM, Vasconcelos DCL, Vasconcelos WL, Nascimento JF, Grava WM, et al. Role of the type of grafting solvent and its removal process on APTES functionalization onto SBA-15 silica for CO2 adsorption. J Porous Mater 2019;26:1581–91. https://doi.org/10.1007/s10934-019-00754-6.

[50] Barczak M, Wierzbicka M, Borowski P. Sorption of diclofenac onto functionalized mesoporous silicas: Experimental and theoretical investigations. Microporous Mesoporous Mater 2018;264:254–64. https://doi.org/10.1016/j.micromeso.2018.01.013.

[51] Bai S, Liu J, Gao J, Yang Q, Li C. Hydrolysis controlled synthesis of amine-functionalized hollow ethane-silica nanospheres as adsorbents for CO_2 capture.

Microporous Mesoporous Mater 2012;151:474–80. https://doi.org/10.1016/j.micromeso.2011.09.014.

[52] Jung HY, Gupta RK, Oh EO, Kim YH, Whang CM. Vibrational spectroscopic studies of sol-gel derived physical and chemical bonded ORMOSILs. J Non Cryst Solids 2005;351:372–9. https://doi.org/10.1016/j.jnoncrysol.2005.01.004.

[53] Yoshino H, Kamiya K, Nasu H. IR study on the structural evolution of sol-gel derived SiO_2 gels in the early stage of conversion to glasses. J Non Cryst Solids 1990;126:68–78. https://doi.org/10.1016/0022-3093(90)91024-L.

[54] Han Y, Lin J, Zhang H. Photoluminescence of organic-inorganic hybrid SiO_2 xerogels. Mater Lett 2002;54:389–96. https://doi.org/10.1016/S0167-577X(01)00599-7.

[55] Ataollahi N, Cappelletto E, Vezzù K, Di Noto V, Cavinato G, Callone E, et al. Properties of anion exchange membrane based on polyamine: Effect of functionalized silica particles prepared by sol–gel method. Solid State Ionics 2018;322:85–92. https://doi.org/10.1016/j.ssi.2018.04.022.

[56] Almeida RM, Pantano CG. Structural investigation of silica gel films by infrared spectroscopy. J Appl Phys 1990;68:4225–32. https://doi.org/10.1063/1.346213.

[57] Basyuk VA. Infrared spectra of carboxylic compounds on silica surfaces at 1500–1800 cm^{-1}. J Appl Spectrosc 1994;60:29–33. https://doi.org/10.1007/BF02606071.

[58] Bianchini D, Barsan MM, Butler IS, Galland GB, dos Santos JHZ, Fasce DP, et al. Vibrational spectra of silsesquioxanes impregnated with the metallocene catalyst bis(η5-cyclopentadienyl)zirconium(IV) dichloride. Spectrochim Acta -

Part A Mol Biomol Spectrosc 2007;68:956–69. https://doi.org/10.1016/j.saa.2007.01.009.

[59] Mallakpour S, Nikkhoo E. Production and characterization of nanocomposites based on poly(amide-imide) containing 4,4′-methylenebis(3-chloro-2,6-diethylaniline) using nano-TiO_2 surface-coupled by 3-aminopropyltriethoxysilane. Prog Org Coatings 2013;76:231–7. https://doi.org/10.1016/j.porgcoat.2012.09.022.

[60] Thielemann JP, Weinberg G, Hess C. Controlled synthesis and characterization of highly dispersed molybdenum oxide supported on silica SBA-15. ChemCatChem 2011;3:1814–21. https://doi.org/10.1002/cctc.201100154.

[61] Hartono SB, Hadisoewignyo L, Yang Y, Meka AK, Antaresti, Yu C. Amine functionalized cubic mesoporous silica nanoparticles as an oral delivery system for curcumin bioavailability enhancement. Nanotechnology 2016;27:505605. https://doi.org/10.1088/0957-4484/27/50/505605.

[62] Bois L, Bonhommé A, Ribes A, Pais B, Raffin G, Tessier F. Functionalized silica for heavy metal ions adsorption. Colloids Surfaces A Physicochem Eng Asp 2003;221:221–30. https://doi.org/10.1016/S0927-7757(03)00138-9.

[63] Abdullah AZ, Sulaiman NS, Kamaruddin AH. Biocatalytic esterification of citronellol with lauric acid by immobilized lipase on aminopropyl-grafted mesoporous SBA-15. Biochem Eng J 2009;44:263–70. https://doi.org/10.1016/j.bej.2009.01.007.

[64] Jung HS, Moon DS, Lee JK. Quantitative analysis and efficient surface modification of silica nanoparticles. J Nanomater 2012;2012:1–8.

https://doi.org/10.1155/2012/593471.

[65] Thommes M, Kaneko K, Neimark A V., Olivier JP, Rodriguez-Reinoso F, Rouquerol J, et al. Physisorption of gases, with special reference to the evaluation of surface area and pore size distribution (IUPAC Technical Report). Pure Appl Chem 2015;87:1051–69. https://doi.org/10.1515/pac-2014-1117.

[66] Calvo A, Joselevich M, Soler-Illia GJAA, Williams FJ. Chemical reactivity of amino-functionalized mesoporous silica thin films obtained by co-condensation and post-grafting routes. Microporous Mesoporous Mater 2009;121:67–72. https://doi.org/10.1016/j.micromeso.2009.01.005.

[67] Maria Chong AS, Zhao XS. Functionalization of SBA-15 with APTES and characterization of functionalized materials. J Phys Chem B 2003;107:12650–7. https://doi.org/10.1021/jp035877+.

[68] Jafari Daghlian Sofla S, James LA, Zhang Y. Insight into the stability of hydrophilic silica nanoparticles in seawater for enhanced oil recovery implications. Fuel 2018;216:559–71. https://doi.org/10.1016/j.fuel.2017.11.091.

[69] Antonio Alves Júnior J, Baptista Baldo J. The behavior of Zeta potential of silica suspensions. New J Glas Ceram 2014;4:29–37. https://doi.org/10.4236/njgc.2014.42004.

[70] Wu Z, Xiang H, Kim T, Chun MS, Lee K. Surface properties of submicrometer silica spheres modified with aminopropyltriethoxysilane and phenyltriethoxysilane. J Colloid Interface Sci 2006;304:119–24. https://doi.org/10.1016/j.jcis.2006.08.055.

[71] Zeleňák V, Halamová D, Almáši M, Žid L, Zeleňáková A, Kapusta O. Ordered

cubic nanoporous silica support MCM-48 for delivery of poorly soluble drug indomethacin. Appl Surf Sci 2018;443:525–34. https://doi.org/10.1016/j.apsusc.2018.02.260.

[72] Borjian S, Saunders J, Chen H, Wu X, Crudden CM, Loock H-P, et al. Silicon-on-insulator ring resonators as micro-optical devices for phosphate sensing. Imaging Appl. Opt. 2017 (3D, AIO, COSI, IS, MATH, pcAOP), Optical Society of America; 2017, p. JTu5A.26.

[73] Baek W, Ha S, Hong S, Kim S, Kim Y. Cation exchange of cesium and cation selectivity of natural zeolites: Chabazite, stilbite, and heulandite. Microporous Mesoporous Mater 2018;264:159–66. https://doi.org/10.1016/j.micromeso.2018.01.025.

[74] Carotenuto G, Camerlingo C. Kinetic investigation of water physisorption on natural clinoptilolite at room temperature. Microporous Mesoporous Mater 2020;302:110238. https://doi.org/10.1016/j.micromeso.2020.110238.

[75] Saeed M, Munir M, Nafees M, Shah SSA, Ullah H, Waseem A. Synthesis, characterization and applications of silylation based grafted bentonites for the removal of Sudan dyes: Isothermal, kinetic and thermodynamic studies. Microporous Mesoporous Mater 2020;291:109697. https://doi.org/10.1016/j.micromeso.2019.109697.

[76] Lagergren S. Zur Theorie der Sogenannten Adsorption Gelöster Stoffe. K Sven Vetenskapsakademiens, Handl 1898;24:1–39.

[77] Hock PE, Zaini MAA. Zinc chloride–activated glycerine pitch distillate for methylene blue removal—isotherm, kinetics and thermodynamics. Biomass

Convers Biorefinery 2020;40:1–12. https://doi.org/10.1007/s13399-020-00828-5.

[78] Disanto AR, Wagner JG. Pharmacokinetics of highly ionized drugs II: Methylene blue—absorption, metabolism, and excretion in man and dog after oral administration. J Pharm Sci 1972;61:1086–90. https://doi.org/10.1002/jps.2600610710.

[79] Pernyeszi T, Farkas R, Kovács J. Methylene blue adsorption study on microcline particles in the function of particle size range and temperature. Minerals 2019;9:555. https://doi.org/10.3390/min9090555.

[80] Bulut Y, Aydın H. A kinetics and thermodynamics study of methylene blue adsorption on wheat shells. Desalination 2006;194:259–67. https://doi.org/10.1016/j.desal.2005.10.032.

[81] Kannan N, Sundaram MM. Kinetics and mechanism of removal of methylene blue by adsorption on various carbons—a comparative study. Dye Pigment 2001;51:25–40. https://doi.org/10.1016/S0143-7208(01)00056-0.

[82] Tehrani-Bagha AR, Nikkar H, Mahmoodi NM, Markazi M, Menger FM. The sorption of cationic dyes onto kaolin: Kinetic, isotherm and thermodynamic studies. Desalination 2011;266:274–80. https://doi.org/10.1016/j.desal.2010.08.036.

[83] Hassani A, Vafaei F, Karaca S, Khataee AR. Adsorption of a cationic dye from aqueous solution using Turkish lignite: Kinetic, isotherm, thermodynamic studies and neural network modeling. J Ind Eng Chem 2014;20:2615–24. https://doi.org/10.1016/j.jiec.2013.10.049.

[84] Pan X, Zhang M, Liu H, Ouyang S, Ding N, Zhang P. Adsorption behavior and

mechanism of acid orange 7 and methylene blue on self-assembled three-dimensional MgAl layered double hydroxide: Experimental and DFT investigation. Appl Surf Sci 2020;522:146370. https://doi.org/10.1016/j.apsusc.2020.146370.

[85] Modesto HR, Lemos SG, Santos MS dos, Komatsu JS, Gonçalves M, Carvalho WA, et al. Activated carbon production from industrial yeast residue to boost up circular bioeconomy. Waste Biomass Manag Valorization 2021;28:24694–705. https://doi.org/10.1007/s11356-020-10458-z.

[86] Po HN, Senozan NM. The Henderson-Hasselbalch equation: Its history and limitations. J Chem Educ 2001;78:1499–503. https://doi.org/10.1021/ed078p1499.

[87] Borisevitch IE, Pascutti PG, Tabak M. Kinetic studies of the photodecomposition of dipyridamole in solution: interaction with lysophosphatidylchofine and bovine serum albumin. Spectrochim Acta 1992;48A:1427–36. https://doi.org/10.1016/0584-8539(92)80150-U.

[88] Morag J, Dishon M, Sivan U. The governing role of surface hydration in ion specific adsorption to silica: an AFM-based account of the Hofmeister universality and its reversal. Langmuir 2013;29:6317–22. https://doi.org/10.1021/la400507n.

[89] de Andrade MB, Guerra ACS, dos Santos TRT, Mateus GAP, Bergamasco R. Innovative adsorbent based on graphene oxide decorated with Fe_2O_3/ZnO nanoparticles for removal of dipyrone from aqueous medium. Mater Lett 2019;238:233–6. https://doi.org/10.1016/j.matlet.2018.11.168.

[90] Springer V, Pecini E, Avena M. Magnetic nickel ferrite nanoparticles for removal of dipyrone from aqueous solutions. J Environ Chem Eng 2016;4:3882–90. https://doi.org/10.1016/j.jece.2016.08.026.

[91] Dinh V-P, Huynh T-D-T, Le HM, Nguyen V-D, Dao V-A, Hung NQ, et al. Insight into the adsorption mechanisms of methylene blue and chromium(iii) from aqueous solution onto pomelo fruit peel. RSC Adv 2019;9:25847–60. https://doi.org/10.1039/C9RA04296B.

FIGURE CAPTIONS

- Figure 1: Typical FTIR spectra taken in this work. Spectra collected for MESO A, MESO A_Gra, and MESO A_Co.

- Figure 2: Typical thermograms collected in this study. TG profiles taken for SBA-16, SBA-16_Co, and SBA-16_Gra.

- Figure 3: N_2 sorption isotherms obtained for the pure silica matrices prepared here. The open and closed symbols are related to the adsorption and desorption branches, respectively.

- Figure 4: Zeta potential curves obtained for pure and amine-loaded silicas. Curves evaluated for MESO A, MESO A_Gra, and MESO A_Co.

- Figure 5: (a) SEM micrographs taken for SBA-16, MESO C, MESO C_Gra, and MESO C_Co. The scale bars displayed in these images correspond to either 100 μm or 1 mm.

- Figure 6: Adsorption curves obtained at pH 4.5 for the pure silica matrices. MB was used as a pollutant in these tests.

- **Figure 7:** Adsorption curves obtained for pure and amine-loaded samples. MB was used as a pollutant in these tests. Adsorption curves obtained at pH 4.5 for the pure silica matrices and at pH 7.5 for the amine-loaded specimens.

- Figure 8: Adsorption curves obtained for MESO C and SBA-16 at pH ranging from 3.0 to 9.0. MB was used as a pollutant in these tests.

- Figure 9: Adsorption curves obtained for MESO C_Co and MESO C_Gra at pH ranging from 3.0 to 9.0. MB was used as a pollutant in these tests.

- Figure 10: Adsorption curves obtained for MESO C and MESO C_Gra at pH ranging from 3.0 to 9.0. DIP was used as a pollutant in these tests. MESO C_Gra displayed a negligible adsorption at pH 3.0 and this is curve is not shown.

- Figure 11: Adsorption cycles of MESO C after regeneration in air at 450 °C for 15 min.

Figure 1

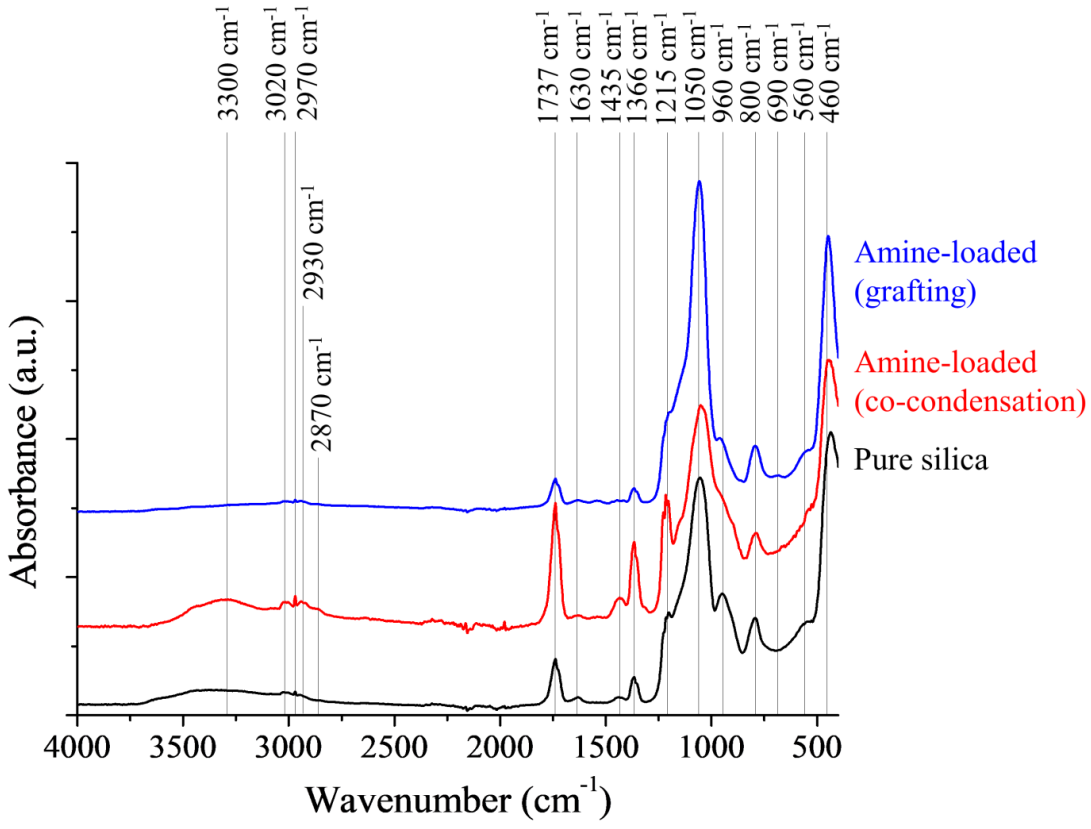

Figure 2

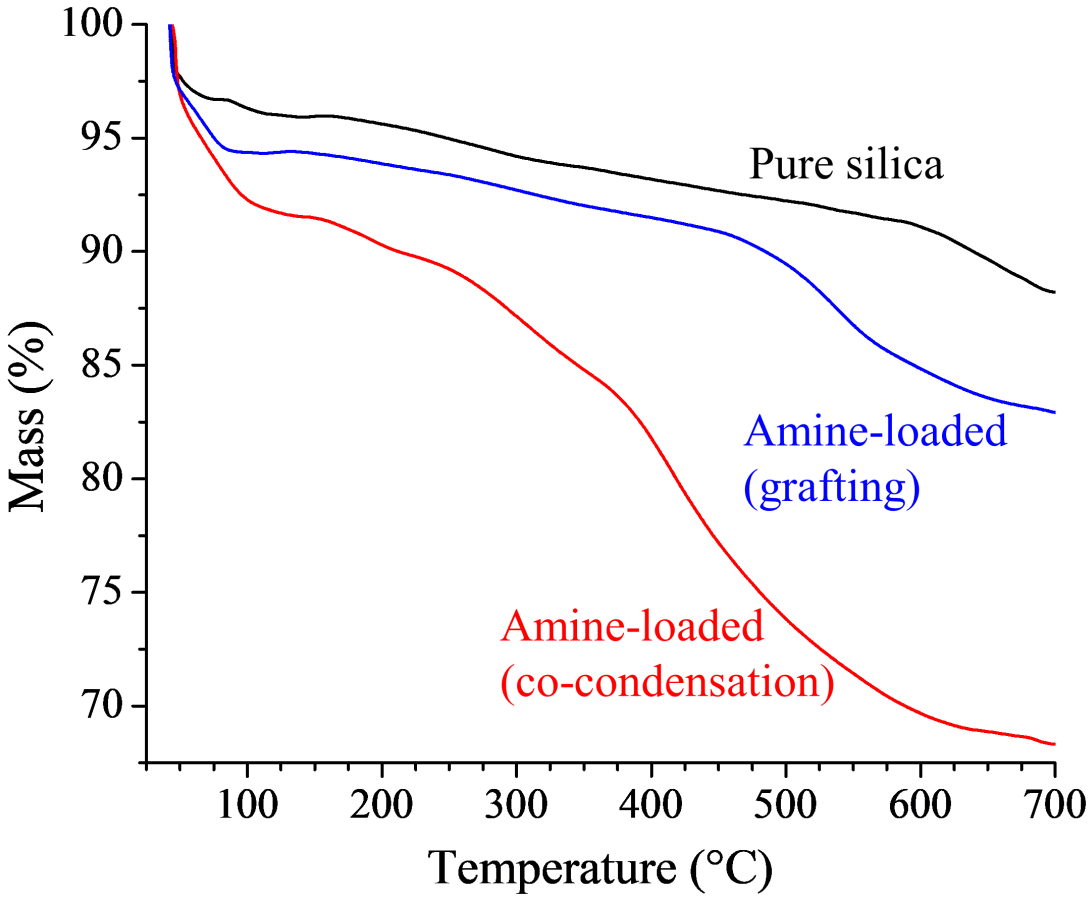
100
95
90
85
80
75
70
Mass (%)
100
200
300
400
500
600
700
Temperature (°C)
Pure silica
Amine-loaded
(grafting)
Amine-loaded
(co-condensation)

Figure 3

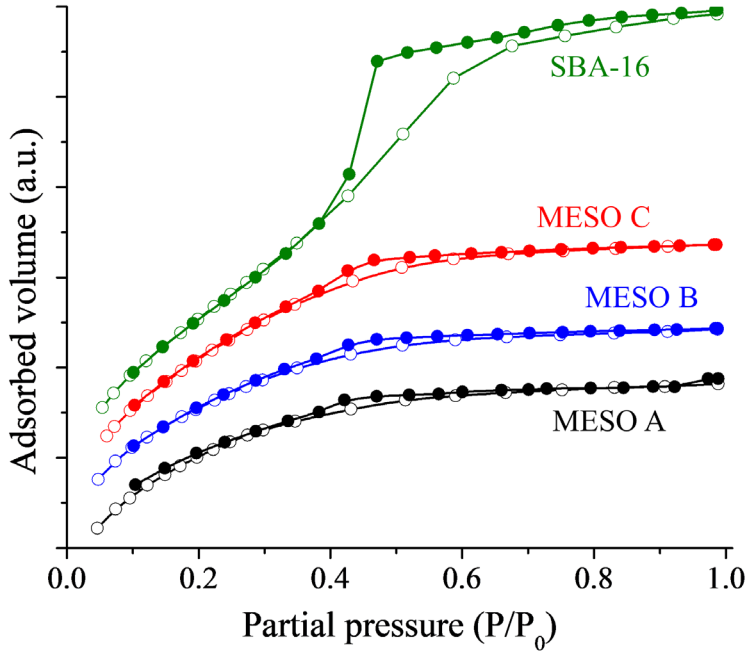

Figure 4

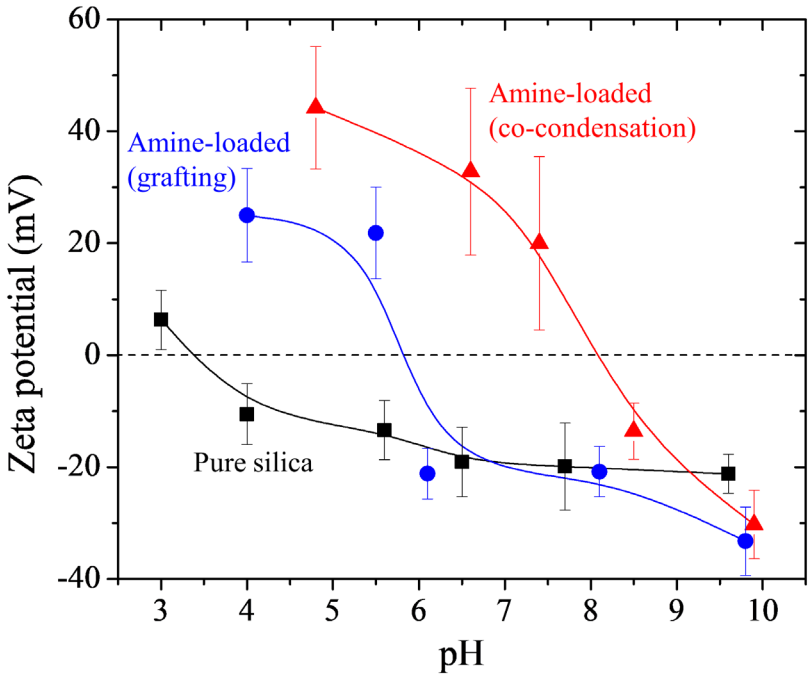

Figure 5

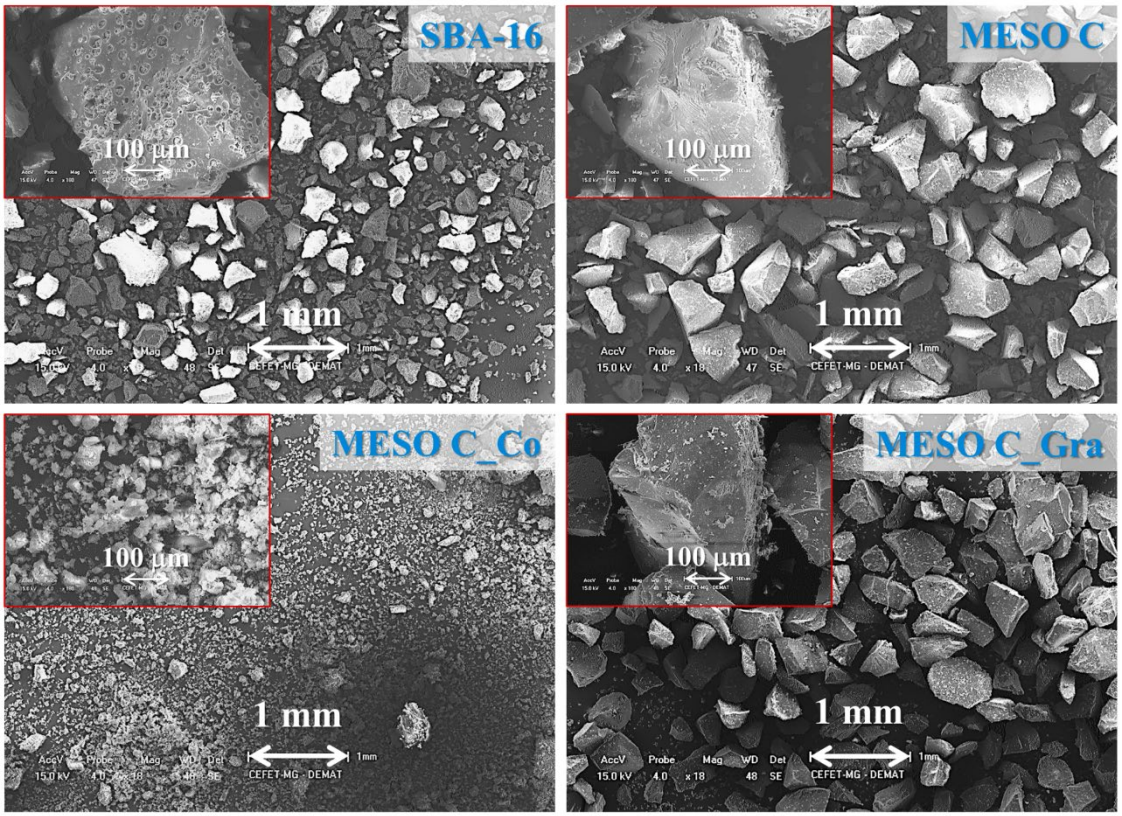

Figure 6

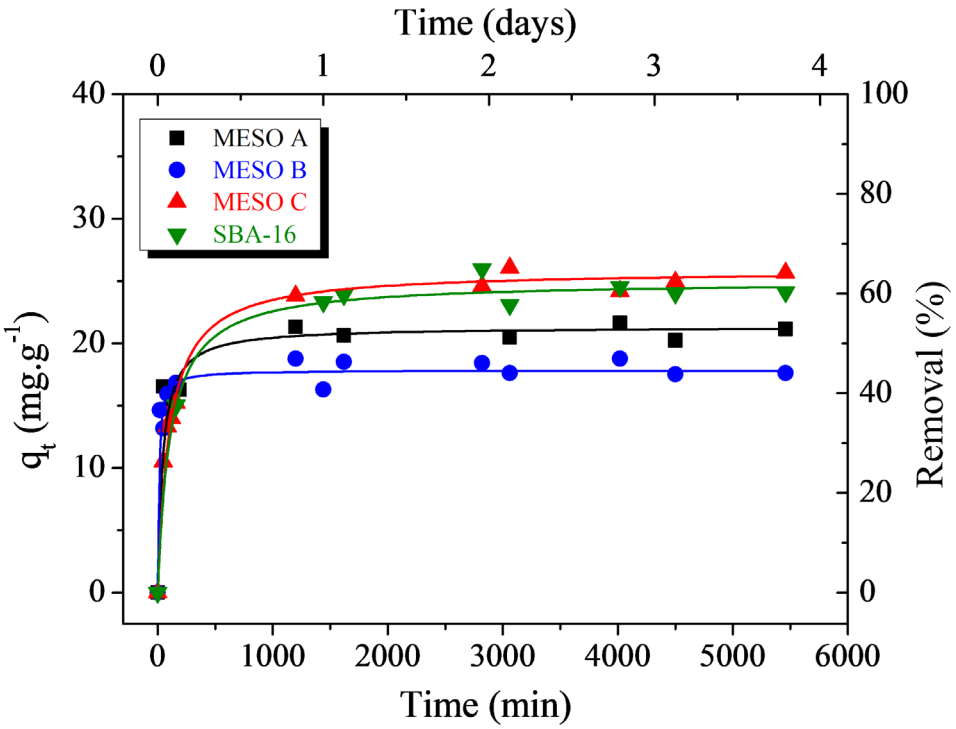

Figure 7

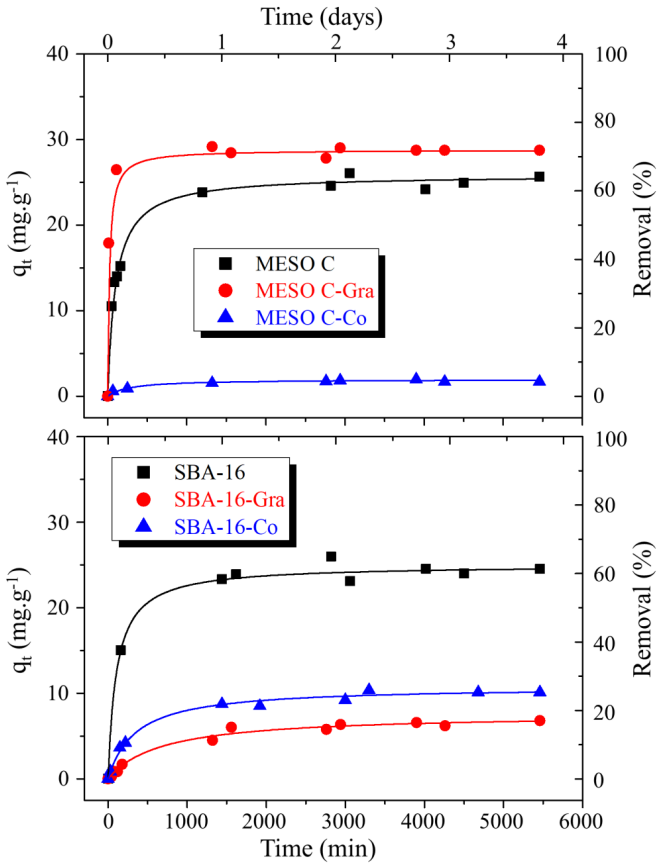
Time (days)
0
1
2
3
4
40
30
20
10
0
100
80
60
40
20
0
q_t (mg.g^{-1})
Removal (%)
MESO C
MESO C-Gra
MESO C-Co
SBA-16
SBA-16-Gra
SBA-16-Co
0
1000
2000
3000
4000
5000
6000
Time (min)

Figure 8

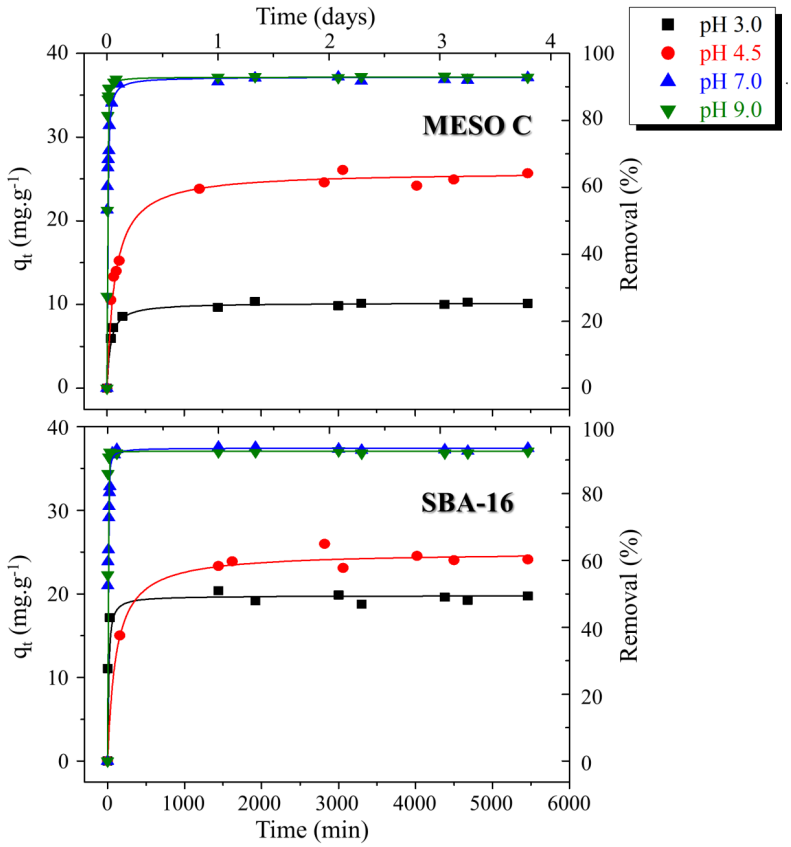
Time (days)
0
1
2
3
4
pH 3.0
pH 4.5
pH 7.0
pH 9.0
MESO C
SBA-16
q_t (mg.g^{-1})
Removal (%)
0
10
20
30
40
0
20
40
60
80
100
0
1000
2000
3000
4000
5000
6000
Time (min)

Figure 9

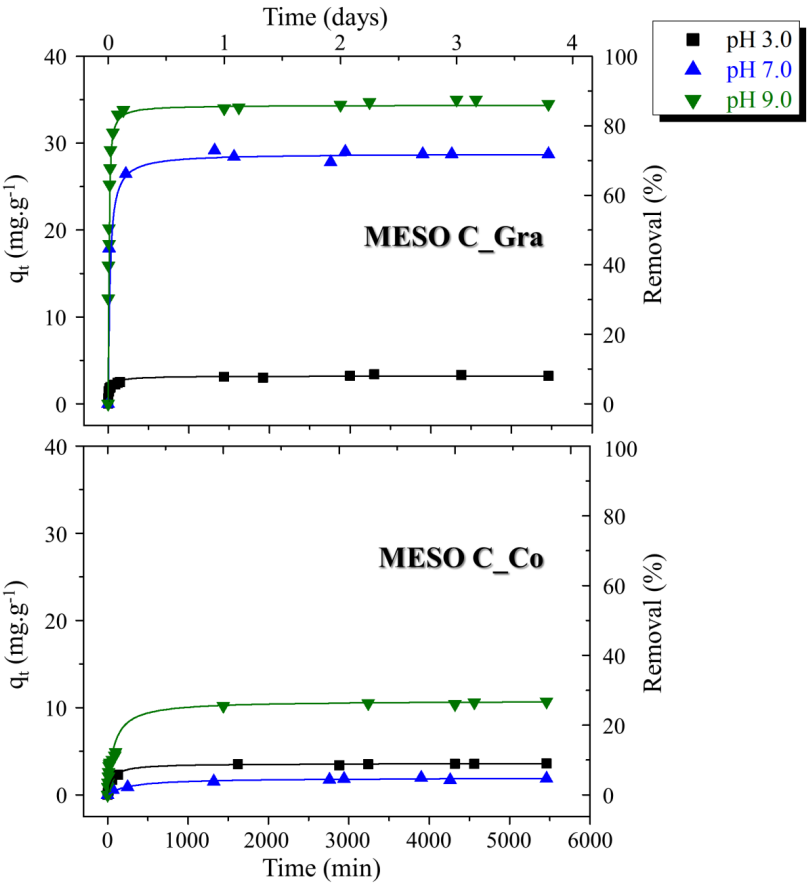
Time (days)
0
1
2
3
4
pH 3.0
pH 7.0
pH 9.0
MESO C_Gra
MESO C_Co
q_t (mg.g^{-1})
Removal (%)
Time (min)
0
1000
2000
3000
4000
5000
6000
10
20
30
40
60
80
100

Figure 10

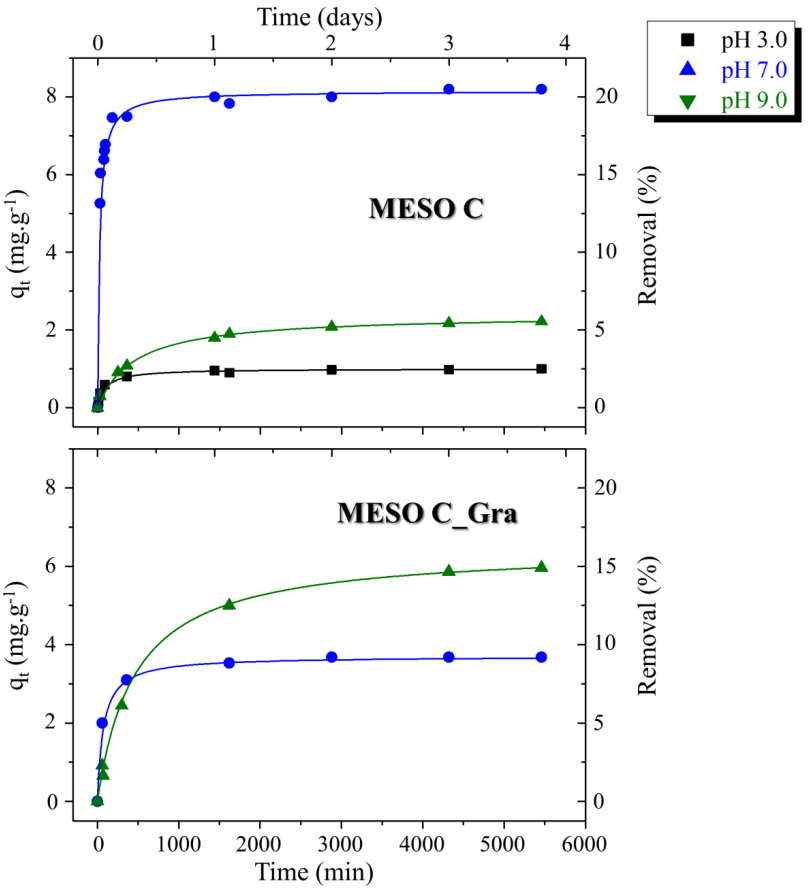

Figure 11